Zonal and Meridional Discontinuities and Other Issues with the HadISST1.1 Dataset

Dudley B. Chelton and Craig M. Risien
College of Earth, Ocean and Atmospheric Sciences
Oregon State University, Corvallis, OR 97331

February 29, 2016

1. Introduction

From November 2013 through 2015, the eastern North Pacific Ocean experienced some of the warmest SST conditions in the historical data record. As shown in Fig. 1 based on anomaly SST fields computed from the Reynolds et al. (2007) Daily Optimal Interpolation dataset (referred to hereafter as OISST), this event first appeared in November 2013 as an area of warm SST in the Northeast Pacific. "The Blob," as it came to be known (Bond et al., 2015), intensified over the next few months and then spread eastward toward the North American continent to span the entire eastern North Pacific. From spring 2014 through the end of 2015, this SST anomaly showed remarkable persistence with very little change in structure.

To determine whether there is any historical precedent for the large-scale anomalous SST in the northeast Pacific, we downloaded the monthly averaged SST fields from the Version 1.1 Hadley Centre Sea Ice and Sea Surface Temperature (HadISST1.1) dataset that is available online from the U.K. Met Office (http://www.metoffice.gov.uk/hadobs/HadISST1.1/). The HadISST1.1 data record extends back to 1870, thus offering a 145-year history of global SST. To our knowledge, this is the longest record of SST available based solely on observations[1]. The HadISST1.1 data are stored on a grid that ranges in longitude from 180°W to 180°E. The "edges" of this dataset thus fall in the middle of the North Pacific. It will be shown in Sec. 3 that this is apparently responsible for one of numerous significant artifacts in the HadISST1.1 dataset.

Before analyzing the HadISST1.1 data, we performed some simple quality control tests to check that it reproduces the well-established large-scale structures of the SST anomaly fields in the North Pacific. The results of this assessment identified several problems that are summarized in Secs. 2–4. Despite these problems, we show that the HadISST1.1 dataset is adequate for many studies of large-scale SST variability. We present an example application in Sec. 5, however, for which the problems identified in Secs. 3 and 4 render the HadISST1.1 dataset inadequate.

2. HadISST1.1 Representation of Large-Scale SST Variability

Maps of anomaly SST from the HadISST1.1 dataset computed over the 1982-2011 time period are generally similar to those from the OISST dataset. This can be seen from Fig. 2, which shows HadISST1.1 maps for the same time period November 2013–October 2015 shown in Fig. 1 from the OISST dataset. There are two significant differences. Firstly, the HadISST1.1 maps are smoother than the OISST maps. This is at least qualitatively expected since the grid resolution of 1°×1° is a factor of four times coarser than the 0.25°×0.25° grid resolution of the OISST fields. For the purposes of investigation of large-scale climate anomalies such as the North Pacific warm "blob" described in the Introduction, the coarser resolution of the HadISST1.1 fields is not a major concern.

[1] The data record for the Extended Reconstructed Sea Surface Temperature (ERSST) dataset produced by the NOAA National Centers for Environmental Information extends back to 1854, but it includes statistical reconstruction of missing data using empirical orthogonal functions.

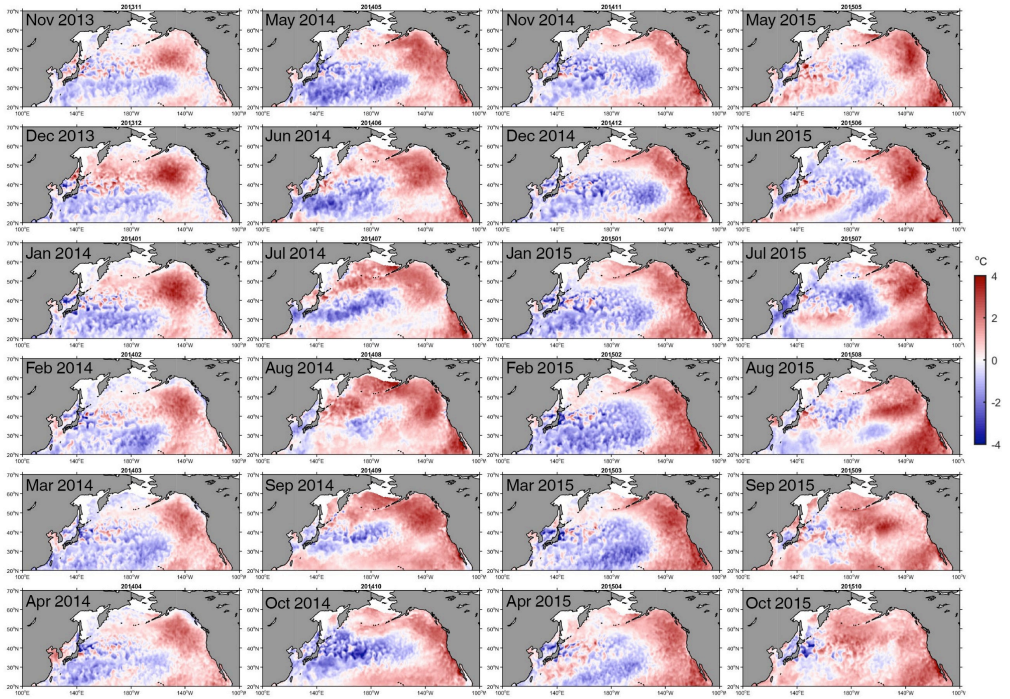

Figure 1. The evolution during the time period November 2013 through October 2015 of SST anomalies computed from the Reynolds et al. (2007) Daily Optimal Interpolation SST dataset (referred to here as OISST) over the time period 1982-2011.

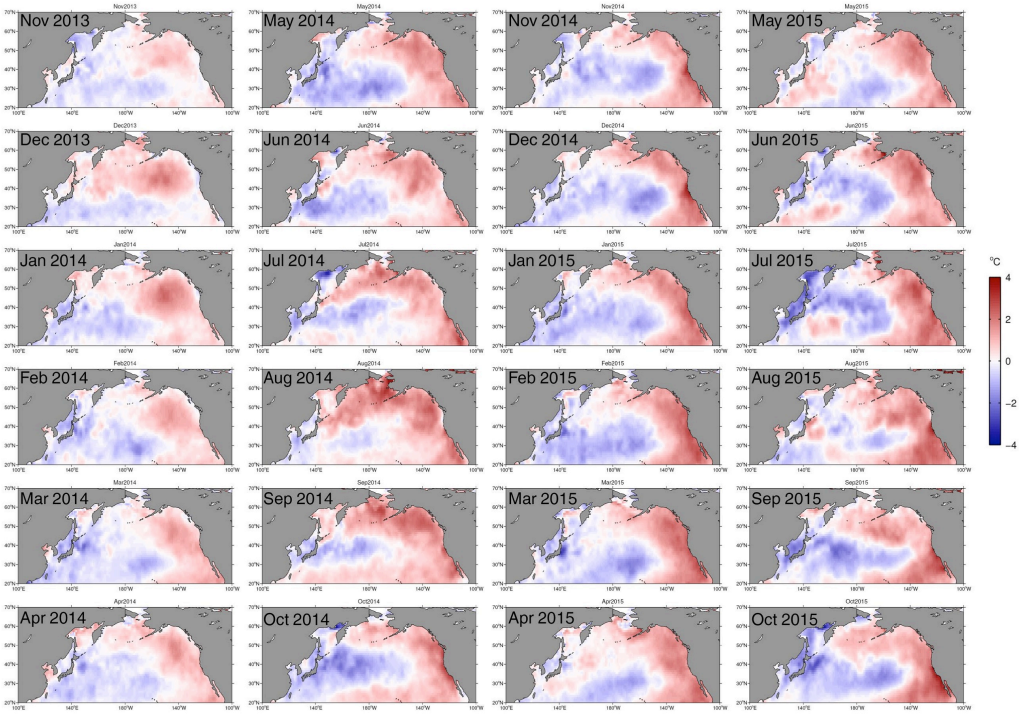

Figure 2. The same as Fig. 1, except the evolution during the time period November 2013 through October 2015 of SST anomalies computed from the HadISST1.1 dataset over the time period 1982-2011. The color bar is the same as that used in Fig. 1.

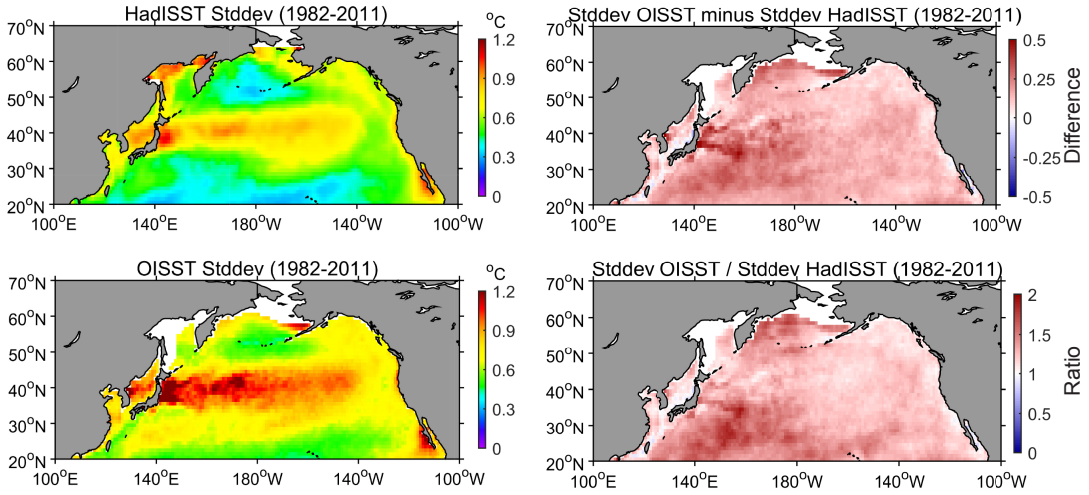

Figure 3. The standard deviations of SST anomalies computed over the time period 1982-2011from the HadISST1.1 dataset (top left) and the OISST dataset (bottom left). The right panels show the differences between the two standard deviations (OISST minus HadISST1.1, top right) and the ratio of the two standard deviations (OISST divided by HadISST1.1, bottom right).

A more important difference is that the magnitudes of the SST anomalies are significantly smaller in the HadISST1.1 dataset than in the OISST dataset. This is visually apparent from the left panels of Fig. 3 as smaller standard deviations of the SST anomalies throughout the North Pacific in the HadISST1.1 dataset compared with the OISST dataset. The low bias of the HadISST1.1 anomalies is quantified in the right panels of Fig. 3. The differences between the standard deviations of SST anomalies (OISST minus HadISST1.1) are about 0.2°C over the eastern half of the North Pacific, increasing to about 0.4°C in the region of the Kuroshio Extension (top right panel). Viewed alternatively, the ratios of the standard deviations of SST anomalies (OISST divided by HadISST1.1) indicate that the OISST anomalies are larger by a factor of about 1.25 over the eastern half of the North Pacific, increasing to more than a factor of 1.75 in the southwestern area of the region shown in Fig. 3. These differences seem larger than could be accounted for solely by the coarser 1°×1° grid resolution of the HadISST1.1 dataset compared with 0.25°×0.25° for the OISST dataset.

While the significantly smaller magnitudes of the SST anomalies are a concern, the HadISST1.1 data could still be useful for studies of short-term climate variability (interannual to decadal time scales), as long as they able to reproduce the spatial patterns of the large-scale climate signals and their temporal variations. To assess the utility of HadISST1.1 data for such studies, we computed the first four empirical orthogonal functions (EOFs) of the anomaly SST fields from both the HadISST1.1 and the OISST datasets over a common time period of 1982-2011.

The spatial patterns of the EOFs and their time variations are quite similar for all four of the EOFs from the two datasets shown in Fig. 4. The existence of more small-scale structure in the EOFs from OISST is again a manifestation of the higher resolution of the OISST fields. The lack of small-scale variability in the HadISST1.1 data also explains the higher percentage of variance accounted for by each EOF compared with the OISST dataset (see the labels in the upper right corner of each amplitude time series plot). As noted above from Figs. 1 and 2, the lack of small-scale features in HadISST1.1 is not a major concern for climate studies.

More rigorous comparisons between the EOFs from the HadISST1.1 and OISST datasets were made from cross correlation analysis. The spatial cross correlations of the EOFs from the two datasets (see caption) are about 0.85-0.90. These correlations are somewhat disappointing, but are probably acceptably high for most climate studies. While the different resolutions of the two datasets are a contributing factor, the reduced spatial cross correlations are mostly attributable to the smaller magnitudes of the HadISST1.1 anomalies, which result in smaller dynamic ranges of the EOF values. This is especially evident from the maps for EOFs 2 and 4, which are the modes with the smallest cross correlations of about 0.85. The temporal cross correlations of the amplitude time series of the EOFs from the two datasets (see caption) are about 0.90 for each mode. Again, these correlations are disappointing but they are probably acceptably high for most climate studies.

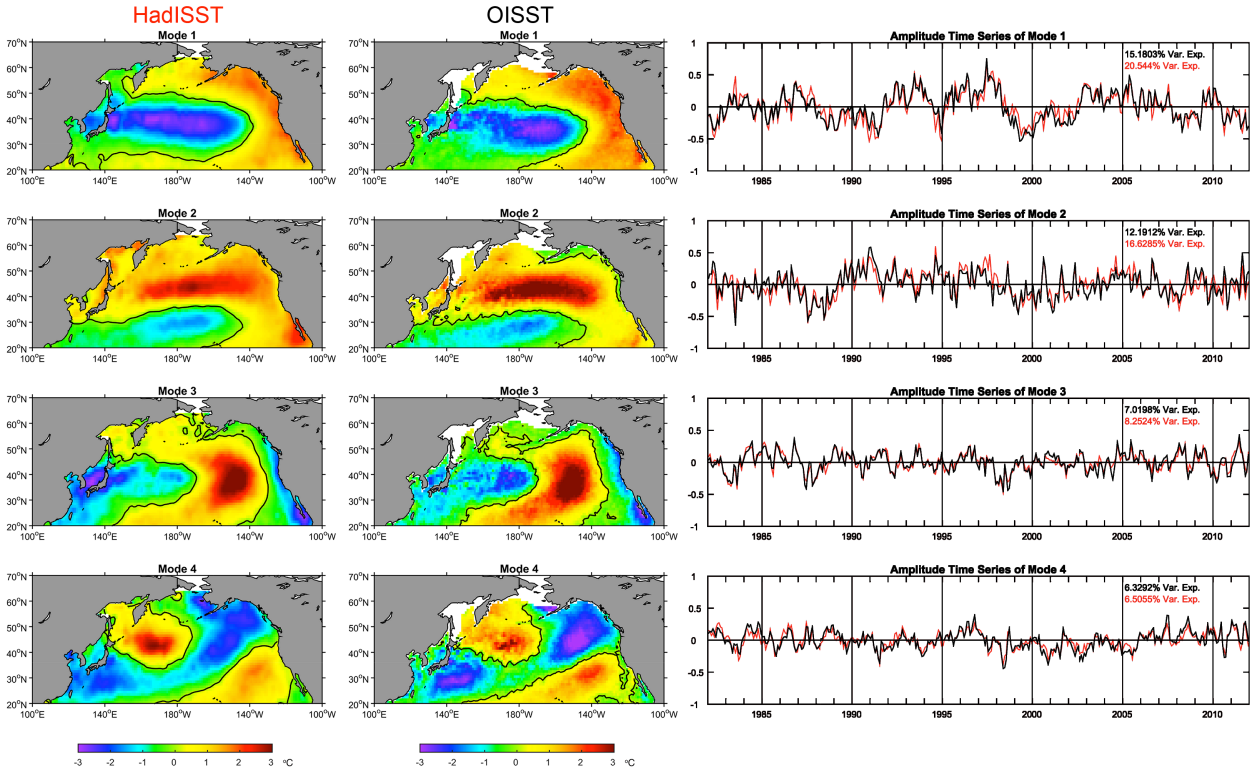

Figure 4. The first four EOFs of SST anomalies computed over the time period 1982-2011 and the corresponding EOF amplitude time series for the HadISST1.1 dataset (left panels and red lines in the time series) and the OISST dataset (middle panels and the black lines in the time series). The cross correlations between the spatial patterns of EOFs 1-4 are, respectively, 0.90, 0.85, 0.91 and 0.84. The cross correlations between the amplitude time series are, respectively, 0.92, 0.88, 0.92 and 0.89.

The similarities of the EOFs in Fig. 4 from HadISST1.1 and OISST are encouraging. We therefore extended the analysis to compute HadISST1.1 anomalies over a longer data record than the restricted period 1982-2015 for which the OISST data are available. Because of concerns about the quality and coverage of data during the early years, we restricted attention to the portion of the data record after 1900. We computed the anomalies of SST over the time period 1910–2005 after removing a linear trend in SST at each 1°×1° grid point. The 10-year truncation at each end of the 1900-2015 data record in our chosen reference period for defining the seasonal cycle for computation of the anomalies was imposed in order to avoid edge effects when

applying a low-pass filter with a 10-year half-power filter cutoff period, which inadvertently identified a problem with the HadISST1.1 dataset that we might not have noticed otherwise (see Fig. 7 below).

From an exploratory analysis of the 1910-2005 anomalies from the HadISST1.1 dataset, we discovered that there are noticeable differences in the character of the data before and after 1949. The magnitudes of the SST anomalies are significantly smaller during the earlier part of the data record than during the later part. This can be seen from Fig. 5, which shows maps of the standard deviations of the SST anomalies for the time periods 1909-1948 (left) and 1949-1988 (right). In the zonal band of maximum variability centered near 40°N, for example, the standard deviation is about 0.8°C in the early part of the data record and about 1.1°C in the later part. Systematic non-stationarity with a magnitude of 0.3°C between the pre-1949 and post-1949 parts of the HadISST1.1 data record exceed the climate research user requirements for accuracies better than 0.1°C (Kaiser-Weiss et al., 2012).

The different magnitudes of the SST anomalies before and after 1949 can be seen in somewhat more detail in Fig. 6 from the time series of spatial standard deviation within the region 180°W-150°W, 35°N-45°N. The notably higher spatial variability beginning in 1949 likely indicates that the resolution of the HadISST1.1 fields increased rather abruptly at that time.

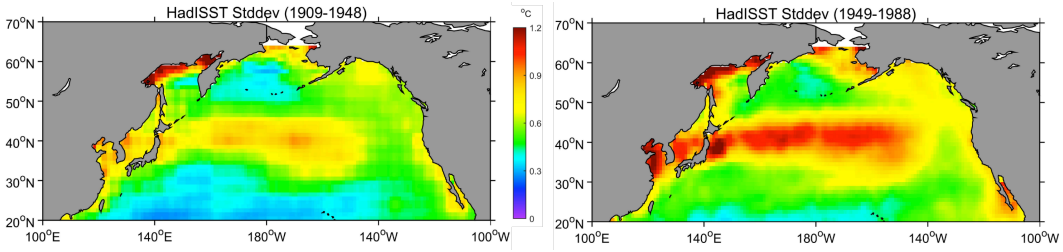

Figure 5. The standard deviations of SST anomalies from the HadISST1.1 dataset computed for two 40-year time periods. The panels on the left and right show, respectivey, the standard deviation for the 1909-1948 and 1949-1988 time periods. The reference time period for defining the anomaly values is 1910-2005.

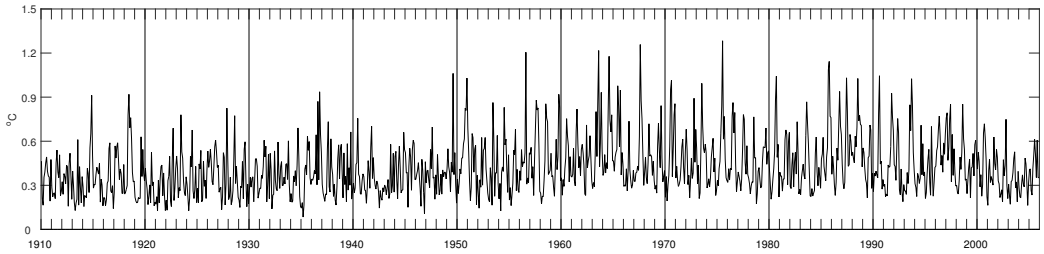

Figure 6. Time series of the spatial standard deviation of SST anomalies within the region 180°W-150°W, 35°N-45°N from the HadISST1.1 dataset.

The spatial patterns of large-scale variability in the HadISST1.1 dataset over the longer time period 1910-2005 are summarized in the left panels of Fig. 7 from the first four EOFs computed from the unfiltered HadISST1.1 anomalies. These EOFs are very similar to the spatial patterns of the EOFs in the left panels of Fig. 4 computed from the HadISST1.1 data over the shorter time period 1982-2011. These EOF indices of large-scale climate variability are thus seen to be quite robust over the 95-year HadISST1.1 data record considered here.

Because we have an interest in the nature of recurring large-scale patterns of SST on different time scales, we recomputed the first four EOFs from the 1910-2005 time period of the

HadISST1.1 data record after low-pass filtering the time series at each grid point with a half-power filter cutoff period of 10 years. This calculation unexpectedly exposed the first of several issues with the details of the mapping procedure used to construct the HadISST1.1 dataset. As shown in the right panels of Fig. 7, a discontinuity is clearly evident just east of the international dateline in EOF #3. To a lesser extent, the problem near the dateline is also evident from close inspection of EOF #1. Enlightened by this result, a subtle meridional stripe of locally smaller standard deviation of the SST anomalies just east of the dateline can be seen retrospectively in the right panel of Fig. 5.

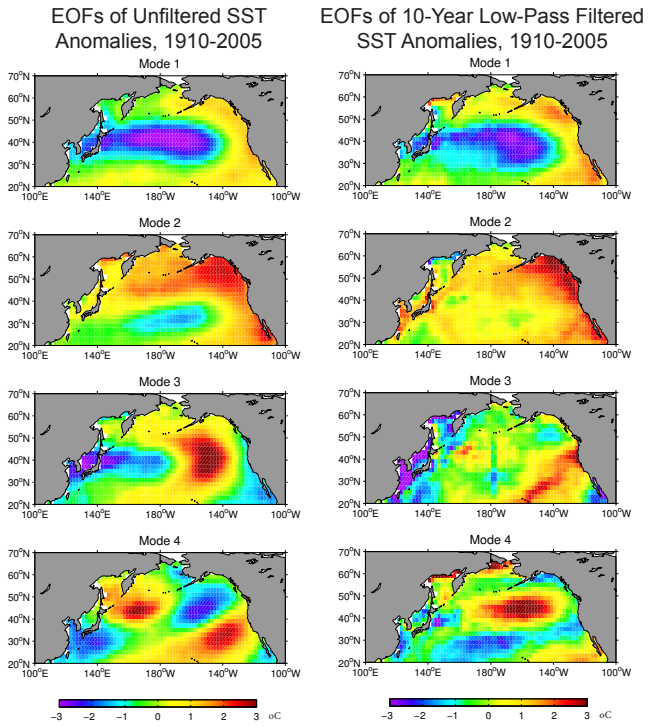

Figure 7. The first four EOFs of SST anomalies computed from the HadISST1.1 dataset for the time period 1910-2005 after removing a linear trend at each grid point. The panels on the left were computed from unfiltered SST anomalies and the panels on the right were computed from SST anomalies after low-pass filtering with a half-power filter cutoff period of 10 years.

To investigate the discontinuity near the dateline in more detail, we computed the average of the anomaly SST at each grid point over two 30-year subrecords of the 1910-2005 time period over which the anomalies were defined. By definition, the average value of the SST anomalies at each grid point is zero over the full time period 1910-2005. However, the average is generally not zero over any particular subrecord. The results are shown in Fig. 8 for a region centered on the dateline for the time periods 1910-1939 (left) and 1950-1979 (right). It is apparent that the average anomalies along 179.5°W are locally positive in the early period and locally negative in the later period. During the later period, the average SST is about 0.2°C cooler along 179.5°W than along the meridians that are 1° of longitude to the west or east.

The abrupt post-1949 decrease of 0.2°C along the 179.5°W meridian compared with the adjacent meridians to the west and east is clearly nonphysical and is thus indicative of a problem with the HadISST1.1 dataset. Systematic errors of this magnitude again exceed the climate

research user requirements for accuracies better than 0.1°C (Kaiser-Weiss et al., 2012). Since the longitude of 179.5°W is close to the western "edge" of the HadISST1.1 dataset, the anomalous behavior is likely an edge effect artifact from the details of the mapping procedure used to generate the HadISST1.1 dataset. Without knowing these details, it is difficult for us to speculate about the cause of the problem. It likely arises somehow from not properly considering the 360° circularity of longitude in the smoothing procedure.

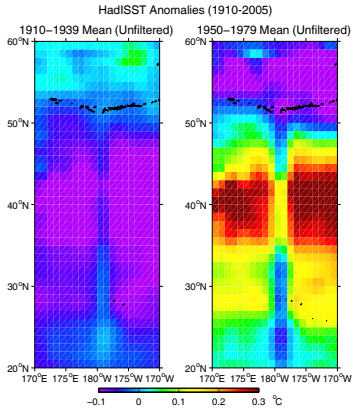

Figure 8. The average value of unfiltered SST anomalies during two 30-year time periods from the HadISST1.1 dataset near the international dateline. Anomaly SST time series were computed over the time period 1910-2005 after removing a linear trend at each grid point. By definition, the average value of the SST anomalies over the full 95-year time period 1910-2005 is zero at every grid point. The two panels show the average values of these SST anomalies over the 1910-1939 (left) and 1950-1979 (right) portions of the 95-year data record.

Besides the discontinuity along 179.5°W, there are numerous other significant differences between the average values of the SST anomalies during the two time periods considered in Fig. 8. For example, except for the meridional band of negative artifact values along 179.5°W, the average values at midlatitudes are much larger during the later time period compared with the early time period. In contrast, the average values at high latitudes are smaller during the later time period. These large-scale features are likely at least partly attributable to sampling issues because of the sparser data coverage in the early years compared with more recent time periods. For present purposes, these differences are probably of secondary importance to the discontinuity just east of the dateline and the additional zonal and meridional discontinuities identified in Secs. 3 and 4 below.

We note that the discontinuity along 179.5°W has been previously documented by other users. The following warning was posted on the U.K. Met Office website on 13 March 2015:

> **13/MARCH/2015. Users have noticed that there is a minor discontinuity at the dateline in HadISST1 SST fields starting in 1982. It appears to only affect gridcells just to the east of the dateline. Please note that this can affect estimates of the mean and variability of SSTs in HadISST1 when analysed across this region.**

Based on the analysis presented above, this warning understates the problems in the HadISST1.1 dataset. While the warning says that the discontinuity just east of the dateline starts in 1982, our analysis indicates that it starts much earlier than this; it appears that this problem first arises in 1949. The analysis in Sec. 3 reveals the existence of additional zonal discontinuities in the HadISST1.1 dataset. Analogous meridional discontinuities are identified in Sec. 4.

3. Zonal Discontinuities in the HadISST1.1 Dataset

In order to gain more insight into the peculiar behavior of SST anomalies just east of the dateline that is evident in Figs. 5, 7 and 8, we computed zonal first-differences of the SST field at each grid point. Based on the right panel of Fig. 8, we expected that the discontinuity at 179.5°W would show up as a pair of meridional stripes of high variance of zonal first differences along the longitudes of 180.5°W and 178.5°W that straddle 179.5°W. As discussed below, however, the zonal first-differences unexpectedly revealed other problems in addition to the discontinuity just east of the dateline.

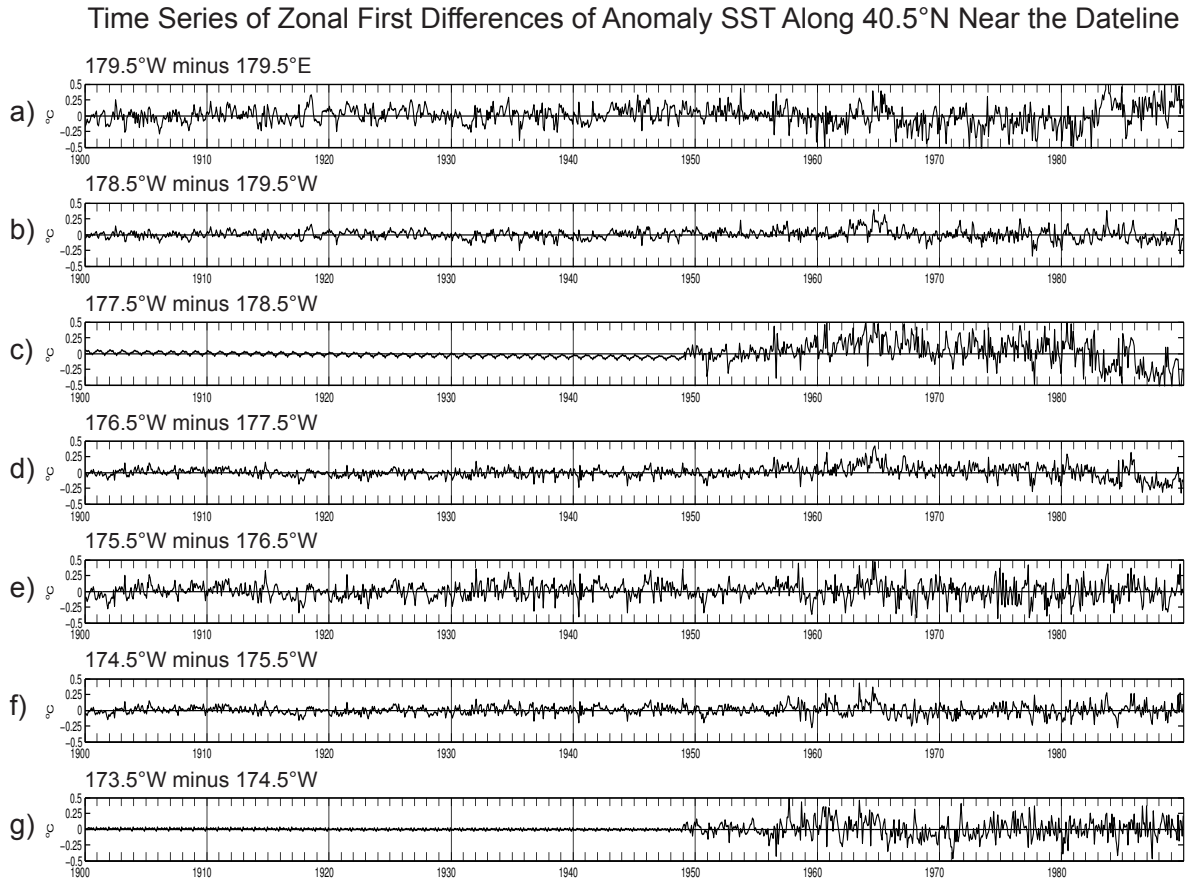

Figure 9. Time series of zonal first-differences of unfiltered SST anomalies between selected adjacent pairs of grid point longitudes along 40.5°N computed from the HadISST1.1 dataset over the time period 1910-2005 after removing a linear trend at each grid point. Enlargements of the 1940-1960 portion of the data record for panels a-c are shown in Fig. 10 below.

Time series of the zonal first-differences are shown in Fig. 9 for six pairs of neighboring longitudes between 179.5°W and 174.5°W. These representative grid locations reveal a host of odd behaviors:

1) The first-difference time series in panels a and e have significantly higher variance than the other four panels.
2) Close inspection also shows that the variance in the first-difference time series in panels a and e are somewhat lower during the earlier part of the data record than during the later

part. The precise time of transition from low to high variance is difficult to discern from these two time series.

3) The first-difference time series in panels b, d and f have smaller variances throughout their data records than do the first-difference time series in panels a and e.

4) The above-noted lower variance in the earlier part of the time series compared with the later part is more easily seen in panels b, d and f than in panels a and e. The change occurs abruptly in 1949.

5) The first-difference time series in panels c and g have almost no variance prior to 1949. This small variability in the first-difference time series implies that the time series at the two adjacent grid points are essentially identical. What little differences there are during the pre-1949 part of the data record at these two locations consists mostly of well-defined seasonal cycles with very small amplitudes and different temporal variations at the two locations. Small trend-like behavior is superimposed on these small-amplitude seasonal variations. This is most apparent as the decreasing trend in panel c.

The above artifacts in the first-difference time series are seen more clearly in Fig. 10, which shows enlargements of the time series in the top three panels of Fig. 9 for the 20-year portion of the data record from 1940 to 1960. Prior to 1949, there is a progressive reduction of the variance in the successive time series from top to bottom with the above-noted seasonality in the early portion of the data record in panel c. Note the abruptness of the change in character of the first-differences of SST anomalies in panel c before and after 1949. After 1949, the variance is significantly higher in panels a and c than in panel b.

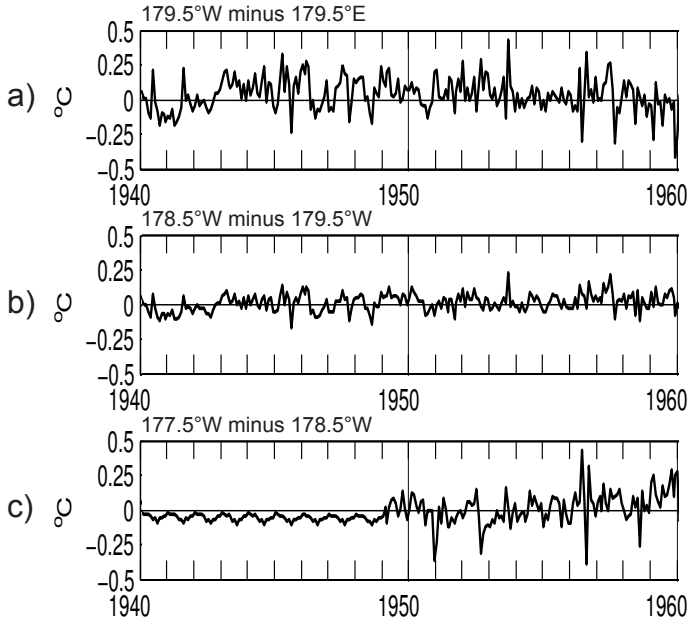

Figure 10. An enlargement of the time series in the top three panels of Figure 9.

The complicated mix of artifacts in the first-difference time series in Figs. 9 and 10 are global in nature. This is summarized in Fig. 11 for the North Pacific region of the HadISST1.1 dataset; the results are similar for the global dataset (not shown here). The figure shows the mean (left panels) and the standard deviation (right panels) of zonal first differences of SST during the pre-

1949 period (top panels) and the post-1949 time period (bottom panels). A non-zero mean discontinuity just east of the dateline after 1949 is clearly evident in the bottom left panel. There are numerous non-zero mean discontinuities before 1949 in the top left panel. The meridional banding of the standard deviations in the right panels has a zonal periodicity of 4° of longitude in the early period and 2° of longitude in the later period. These differences in the zonal periodicities between the early and later parts of the data record were noted above from the example time series in Fig. 9. Note also the higher standard deviations during the later period in the bottom right panel compared with the earlier period in the top right panel. This is consistent with the larger standard deviations of SST anomalies after 1949 compared with the earlier time period discussed above from Fig. 5. We previously speculated that this may be attributable to the higher quality and better coverage of the observations during the later part of the data record.

The different periodicities in the standard deviations of the zonal first-differences of SST are shown in detail along 40.5°N in Fig. 12. Consistent with the description above from the example time series in Fig. 9, the "zig-zag patterns" have periodicities of 4° and 2° of longitude in, respectively, the earlier and later parts of the data record (top and bottom panels, respectively). The amplitudes of the zonally oscillating striations in the standard deviations of zonal first differences over the longitude range along 40.5°N shown in Fig. 12 are approximately 0.1°C prior to 1949 and approximately 0.05°C after 1949. The zonally oscillating amplitudes are larger in the far western North Pacific (see Fig. 11). During the latter time period, the magnitudes of the elevated variability are about twice as large on each side of the discontinuity near the dateline. There is no evidence of a discontinuity near the dateline prior to 1949.

The first-difference analysis summarized in Figs. 9-12 thus reveals that the HadISST1.1 dataset is contaminated by a variety of different types of zonal discontinuities.

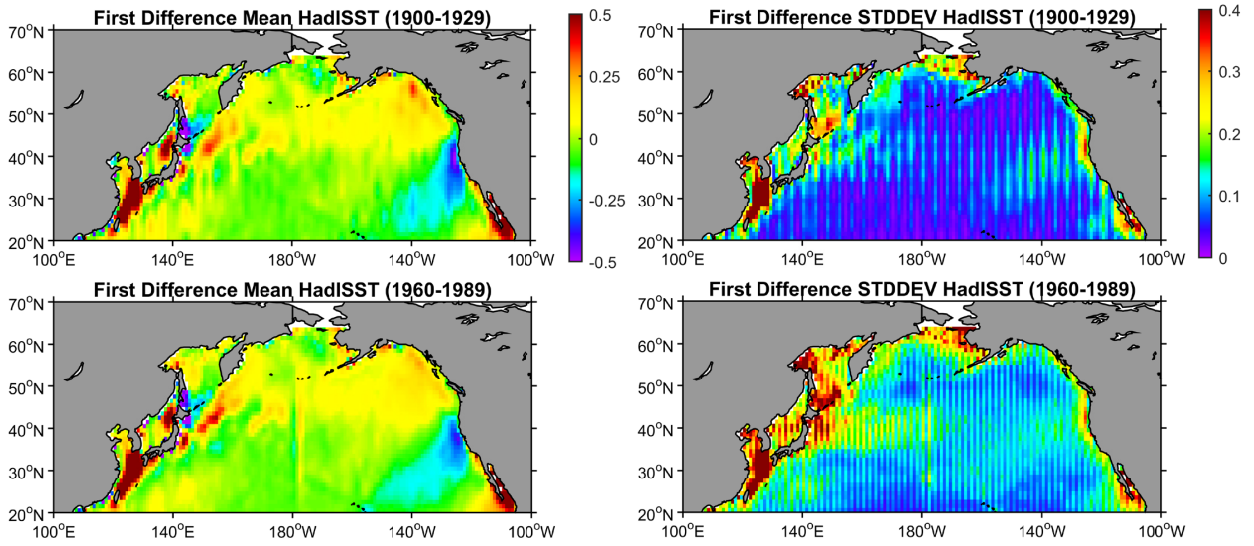

Figure 11. The mean values (left) and standard deviations (right) of zonal first differences of SST anomalies computed from the HadISST1.1 dataset after removing a linear trend at each grid point over the time period 1910-2005. The top and bottom panels were computed from, respectively, the 1900-1929 and 1960-1989 portions of the 95-year data record. The different zonal periodicities of the standard deviations of zonal first differences during the early and later parts of the data record are clearly evident from the meridional stripiness with a periodicities of 4° of longitude prior to 1949 (top right panel) and 2° of longitude after 1949 (bottom right panel).

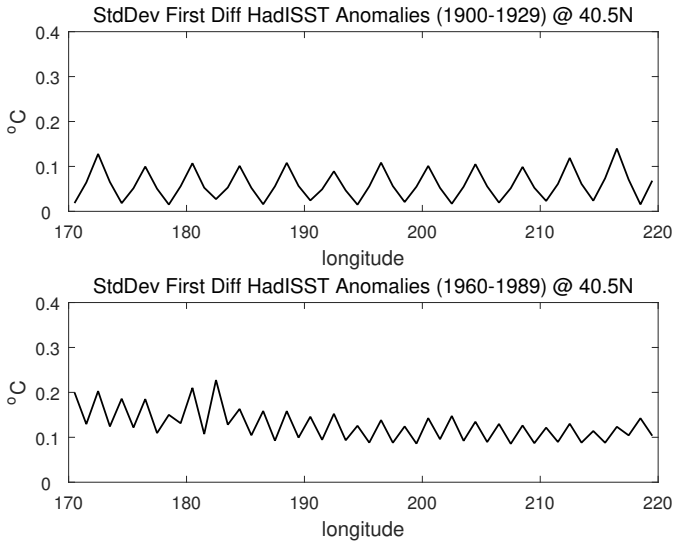

Figure 12. Zonal sections along 40.5°N of the standard deviations of zonal first differences of SST anomalies shown in Fig. 11. The top and bottom panels are for, respectively, the 1900-1929 and 1960-1989 portions of the 95-year data record. The different zonal periodicities of the standard deviations for the parts of the data record before and after 1949 are clearly evident from the "zig-zag patterns" with periodicities of 4° and 2° of longitude in the top and bottom panels, respectively.

It is perhaps difficult to visualize how the problems summarized above from the zonal first difference time series will be manifest in the SST fields themselves. A small standard deviation of the first differences between two neighboring longitudes means that the two SST time series are essentially the same. The periodic structures in the standard deviations of the time series of zonal first differences at 4° intervals of longitude during the early part of the data record and 2° of longitude in the later part of the data record thus imply step-like structures in the standard deviations of the SST fields themselves. These steps are subtle in the standard deviations of the SST but are very clear in the standard deviations of zonal first differences of SST. The magnitudes of the jumps of the standard deviations between these steps are small (typically 0.1°C prior to 1949 and 0.05°C after 1949), but they are clearly artifacts that can impact some applications of the HadISST1.1 dataset. An example of such an application is given in Sec. 5.

4. Meridional Discontinuities in the HadISST1.1 Dataset

The focus of the analysis in Sec. 3 on the zonal discontinuities in the HadISST1.1 dataset was motivated by the discovery in our early analysis that there was a discontinuity along 179.5°W in the 1st and 3rd EOFs of 10-year low-pass filtered SST anomalies (see the right panels of Fig. 7). As described in Sec. 3, our efforts to understand the nature of this zonal discontinuity inadvertently stumbled upon the existence of zonal discontinuities at intervals of 4° and 2° of longitude during, respectively, the pre-1949 and post-1949 periods of the HadISST1.1 data record.

Our subsequent analysis of the HadISST1.1 dataset discovered the existence of meridional discontinuities that are very similar in nature to the zonal discontinuities. As shown from the maps and meridional sections in Figs. 13 and 14, there are meridional discontinuities at intervals of 4° and 2° of latitude during, respectively, the pre-1949 and post-1949 portions of the HadISST1.1 data record, i.e., the same increments in degrees as the zonal discontinuities

identified in Sec. 3. The amplitudes of the meridionally oscillating striations in the standard deviations of meridional first differences are about 0.15°C prior to 1949 (larger than the ~0.1°C amplitude of oscillations of the standard deviations of zonal first differences) and approximately 0.05°C after 1949 (about the same as the amplitudes of the oscillations of the standard deviations of zonal first differences).

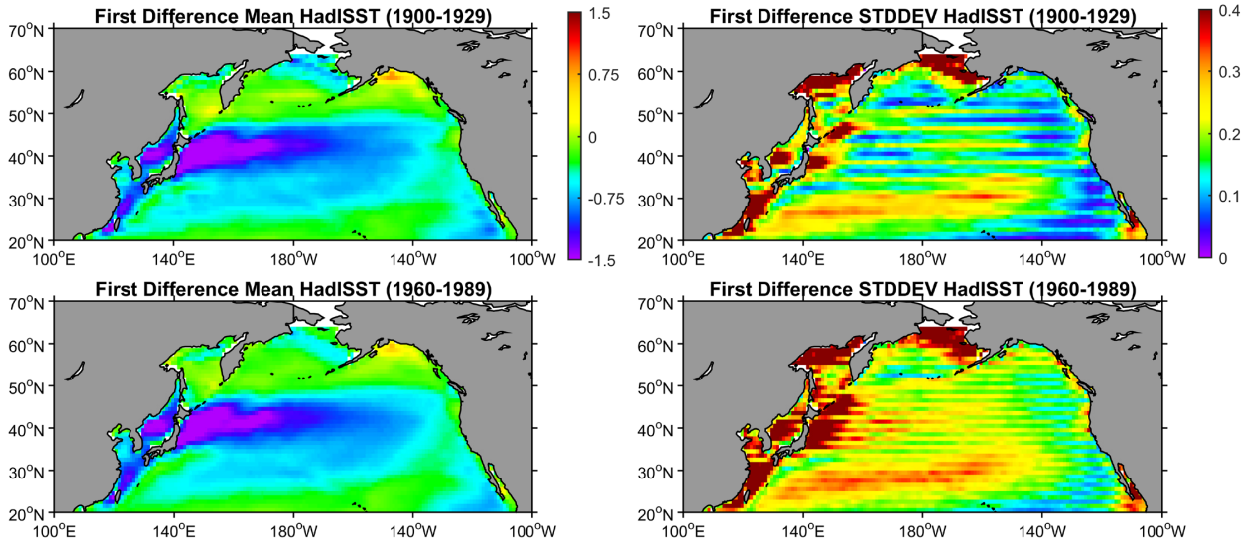

Figure 13. The same as Fig. 11, except the mean values (left) and standard deviations (right) of meridional first differences of SST anomalies computed from the HadISST1.1 dataset after removing a linear trend at each grid point over the time period 1910-2005. The top and bottom panels were computed from, respectively, the 1900-1929 and 1960-1989 portions of the data record. There are no obvious non-zero mean discontinuities in the left panels during either time period. The different meridional periodicities of the standard deviations of meridional first differences during the early and later parts of the data record are clearly evident from the zonal stripiness with a periodicities of 4° of latitude prior to 1949 (top right panel) and 2° of latitude after 1949 (bottom right panel).

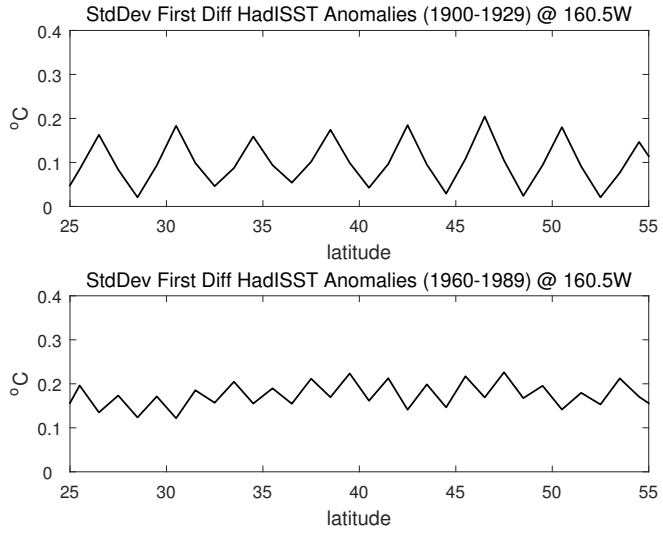

Figure 14. The same as Fig. 12, except meridional sections along 160.5°W of the standard deviations of meridional first differences of SST anomalies shown in Fig. 13. The top and bottom panels are for, respectively, the 1900-1929 and 1960-1989 portions of the 95-year data record. The different meridional periodicities of the standard deviations for the parts of the data record before and after 1949 are clearly evident from the "zig-zag patterns" with periodicities of 4° and 2° of latitude in the top and bottom panels, respectively.

5. An Attempt to Investigate Mesoscale Air-Sea Interaction from the HadISST1.1 Dataset

The discontinuities in the zonal and meridional first-difference SST fields summarized in Secs. 3 and 4 are indicative of a checkerboard pattern of step-like structures in the SST fields themselves. These steps are subtle in the standard deviations of SST, but are very clear in the standard deviations of zonal and meridional first differences of SST in Figs. 11-14. The magnitudes of the jumps of the standard deviations between these steps are relatively small (0.1°-0.15°C prior to 1949 and about 0.05°C after 1949), but they are clearly artifacts in the HadISST1.1 dataset. Moreover, errors of these magnitudes exceed the accuracy requirements for climate data records (Kaiser-Weiss et al., 2012).

The discontinuities in the zonal and meridional first difference SST fields may be a secondary concern for applications in many studies of large-scale signals related to short-term climate variability. Indeed, the fact that these problems have not heretofore been identified by other users attests to that. For studies that require knowledge of the SST gradient field, however, the discontinuities render the HadISST1.1 dataset unusable. An example of such an application is given in this section.

One of the great successes of satellite scatterometry has been the discovery of the ubiquity of the covariability between features in the SST field with scales of 100–1000 km (referred to here as oceanic mesoscales) and surface winds in regions of strong SST fronts throughout the world ocean. The details of this air-sea interaction have been extensively documented in the peer-reviewed literature (see, for example, the reviews by Chelton et al., 2004; Xie, 2004; Small et al., 2008; and O'Neill et al., 2010). On scales smaller than about 1000 km, surface wind speed is positively correlated with SST. The mechanism for this ocean-atmosphere coupling can be briefly summarized as follows. Warm SST decreases the stability of the atmospheric boundary layer, thus mixing momentum downward to the sea surface and resulting in increased surface wind speed anomalies. Cold SST stabilizes the atmospheric boundary layer, thus decoupling the surface winds from the winds aloft and resulting in decreased surface wind speed anomalies.

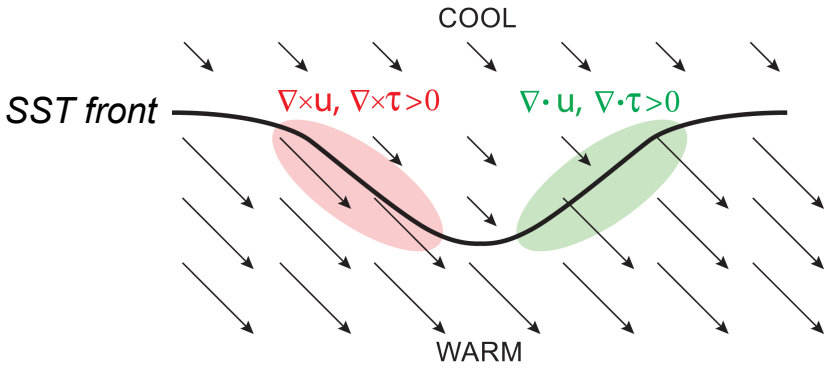

Figure 15. Schematic illustration of the divergence and curl of the vector wind and wind stress fields that result from spatial variations of the SST field. Near a meandering SST front (the heavy black line), surface winds are lower over cool water and higher over warm water, shown qualitatively by the lengths of the vectors. Acceleration where winds have a component across the SST front generates divergence (green area). Lateral variations where winds have a component parallel to the SST front generate curl (red area). The divergence and curl perturbations are found to be linearly proportional to the downwind and crosswind components of the SST gradient, respectively.

A consequence of this SST influence on surface winds is that spatial variability of SST generates divergence and curl of the surface vector wind field (Fig. 15). Divergence can generate vertical motion in the atmosphere and the wind stress curl is the primary forcing of ocean circulation. O'Neill et al. (2010) have shown that the divergence of surface wind and stress both vary linearly with the downwind component of the SST gradient; the curl of surface wind and stress likewise both vary linearly with the crosswind component of the SST gradient.

The vector SST gradient field thus plays a critical role in the coupling between SST and the surface wind field on oceanic mesoscales. The discontinuities in the zonal and meridional first differences summarized in Sections 3 and 4 are clearly an issue for calculation of the spatial derivatives required to determine the zonal and meridional components of the vector SST gradient field.

To illustrate the problem, a monthly seasonal cycle of surface vector winds was computed from the NOAA National Centers for Environmental Prediction (NCEP) Reanalysis I wind fields for the time period 1960-1989. This 12-month seasonal cycle climatology was used to define a climatological average vector wind direction for each corresponding month of the HadISST1.1 dataset. The vector SST gradient field for each month was then computed at each grid point by the usual 3-point centered differencing in each dimension. The zonal (x) and meridional (y) derivatives of SST at grid point (m,n) were thus defined to be

$$T_x(m,n) = [T(m+1,n) - T(m-1,n)]/(2\Delta x)$$

$$T_y(m,n) = [T(m,n+1) - T(m,n-1)]/(2\Delta y),$$

where the subscripts x and y on the left sides of the equations denote differentiation and Δx and Δy are the grid spacings in the zonal and meridional directions. For the HadISST1.1 dataset, Δx = 1° of longitude and Δy = 1° of latitude. The vector SST gradient at grid point (m,n) is

$$\nabla \mathrm{T}(m,n) = \mathbf{i}\, T_x(m,n) + \mathbf{j}\, T_y(m,n),$$

where **i** and **j** are unit vectors in the eastward and northward directions. The downwind and crosswind components of this SST gradient for each month of the HadISST1.1 dataset were computed as, respectively, the dot product and the vertical component of the cross product of $\nabla \mathrm{T}(m,n)$ with a unit vector in the direction of the climatological average seasonal cycle wind vector at grid point (m,n) for the corresponding month.

Maps of the standard deviations of the resulting downwind and crosswind SST gradient fields are shown in Fig. 16. The expected checkerboard patterns from the effects of the 4° zonal and meridional periodicities of first differences prior to 1949 are clearly evident in the top panels. But, except near the international dateline, the expected checkerboard patterns with 2° zonal and meridional periodicities after 1949 are not readily apparent in the bottom panels. This is because the 2° zonal and meridional spacing of the grid points used in the derivative estimates based on 3-point centered differences matches the 2° zonal and meridional spacing of the discontinuities in the first-difference SST fields in Figs. 11-14. Differences are therefore never computed between adjacent corrupted and non-corrupted grid points in the HadISST1.1 dataset when the derivatives are estimated using 3-point centered differencing.

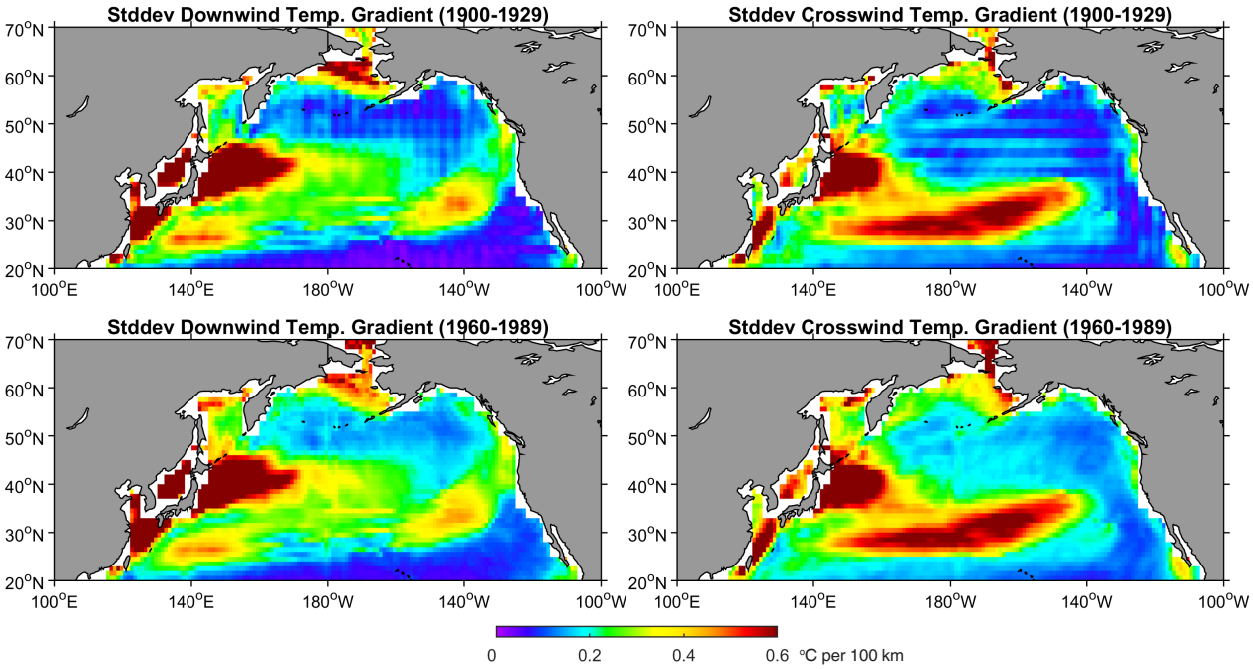

Figure 16. The standard deviations of the downwind (left panels) and crosswind (right panels) components of the SST gradient field computed from the total SST fields (i.e., not the anomaly SST fields) using 3-point centered differences for the derivative components. The wind direction for each month was defined based on the climatological average seasonal cycle of the NCEP Reanalysis I vector wind fields computed over the time period 1960-1989. The standard deviations of SST gradient components in the top and bottom panels were computed from, respectively, the 1900-1929 and 1960-1989 portions of the HadISST1.1 data record.

An alternative procedure for estimating derivative fields with higher spatial resolution than is achieved with the usual 3-point centered differences is to compute 2-point first differences on a staggered grid, as shown schematically in Fig. 17. The first step is to compute the x and y derivatives at the midpoints of the line segments between the corner points as

$$
\begin{aligned}
T_x(m{+}\tfrac{1}{2},n) &= [T(m{+}1,n){-}T(m,n)]/\Delta x \\
T_x(m{+}\tfrac{1}{2},n{+}1) &= [T(m{+}1,n{+}1){-}T(m,n{+}1)]/\Delta x \\
T_y(m,n{+}\tfrac{1}{2}) &= [T(m,n{+}1){-}T(m,n)]/\Delta y \\
T_y(m{+}1,n{+}\tfrac{1}{2}) &= [T(m{+}1,n{+}1){-}T(m{+}1,n)]/\Delta y,
\end{aligned}
$$

where $m{+}\tfrac{1}{2}$ is shorthand notation for the location of the midpoint between grid points m and $m{+}1$ and $n{+}\tfrac{1}{2}$ is the location of the midpoint between grid points n and $n{+}1$. The color coding of the variables matches the colors in Fig. 17. The SST gradient vector on a staggered grid was computed at the midpoint of the cell from the averages of the derivatives on the sides of the cell,

$$
\nabla T(m{+}\tfrac{1}{2},n{+}\tfrac{1}{2}) = \mathbf{i}\,[T_x(m{+}\tfrac{1}{2},n) + T_x(m{+}\tfrac{1}{2},n{+}1)]/2 + \mathbf{j}\,T_y(m,n{+}\tfrac{1}{2}) + T_y(m{+}1,n{+}\tfrac{1}{2})]/2.
$$

The climatological average seasonal cycle wind vector at the staggered grid point ($m{+}\tfrac{1}{2}$, $n{+}\tfrac{1}{2}$) was defined to be the average of the vector winds at the four surrounding grid points (m,n), ($m{+}1$,n), (m,$n{+}1$) and ($m{+}1$,$n{+}1$). The downwind and crosswind components of the SST gradient were computed as before as the dot product and the vertical component of the cross product of $\nabla T(m{+}\tfrac{1}{2},n{+}\tfrac{1}{2})$ with a unit vector in the direction of the climatological vector wind at grid point ($m{+}\tfrac{1}{2}$,$n{+}\tfrac{1}{2}$).

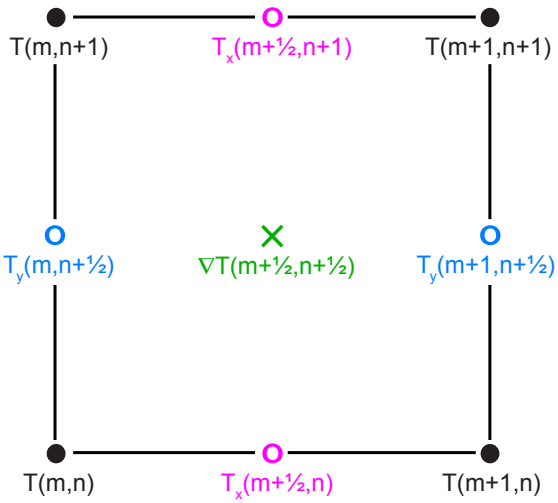

Figure 17. An example 1°×1° grid cell with corners consisting of SST values T at zonal grid points m and m+1 and meridional grid points n and n+1. The components T_x and T_y of the SST gradient vector were computed at the midpoints of the line segments between the corner grid points of the cell. The SST gradient vector ∇T was then computed at the center of the cell, labeled as grid point (m+½,n+½), from the averages of the two adjacent values of T_x and the two adjacent values of T_y. The gridded values of ∇T are seen to be on a 1°×1° latitude-longitude grid that is staggered by 0.5° of latitude and 0.5° of longitude relative to the original 1°×1° grid of SST values.

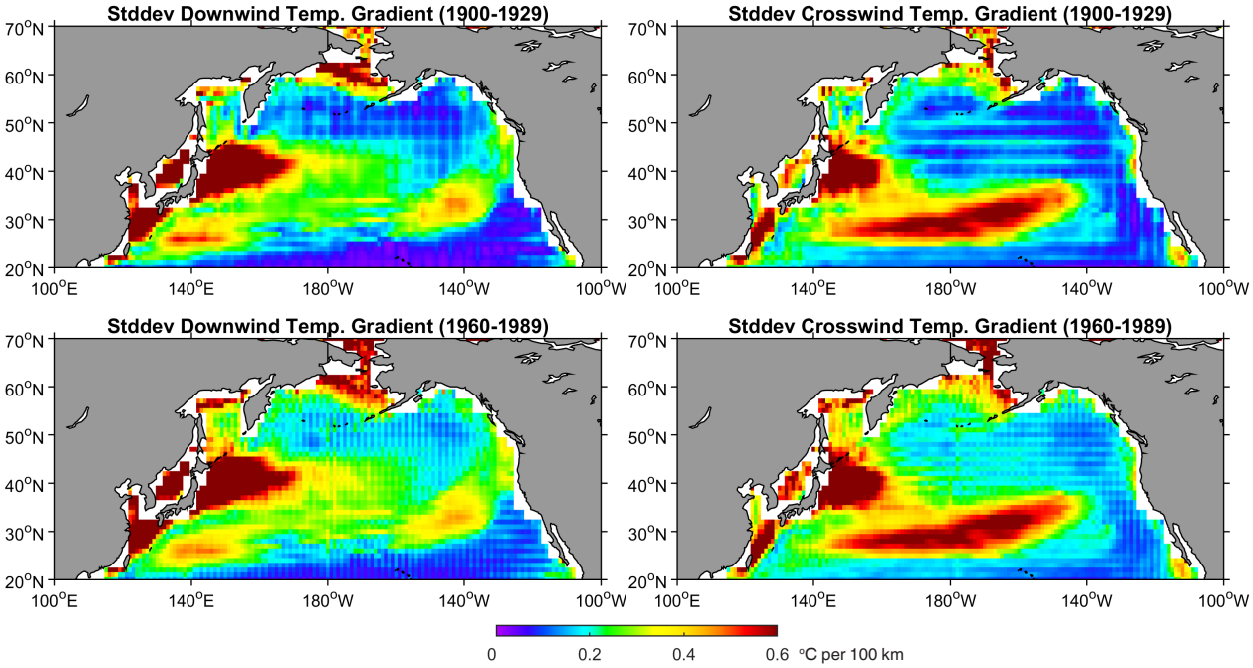

Figure 18. The same as Fig. 16, except the standard deviations of the downwind (left panels) and crosswind (right panels) components of the SST gradient field computed from the total SST fields using 2-point first differences for the derivative components on the staggered grid shown in Fig. 17. As in Fig. 16, the wind direction for each month was defined based on the climatological average seasonal cycle of the NCEP Reanalysis I vector wind fields computed over the time period 1960-1989. The standard deviations of SST gradient components in the top and bottom panels were computed from, respectively, the 1900-1929 and 1960-1989 portions of the HadISST1.1 data record.

Maps of the standard deviations of the higher-resolution downwind and crosswind SST gradient fields on the staggered grid computed from 2-point first differences are shown in Fig. 18. Because of the higher resolution of 2-point first differences compared with 3-point centered differences, the expected checkerboard pattern from the effects of the 4° zonal and meridional periodicities of first differences prior to 1949 are more precisely defined than in Fig. 16. The higher-resolution 2-point first difference estimates of derivatives also clearly reveal the checkerboard pattern from the effects of zonal and meridional periodicities of 2° after 1949 in the bottom panels.

6. Summary and Conclusions

From a detailed analysis of the HadISST1.1 dataset, we have identified numerous problems, some of which limit the utility of the dataset for certain scientific applications. The issues identified from our analysis are:

1) The HadISST1.1 maps are much smoother than maps of SST from the Reynolds et al. (2007) OISST dataset. This is attributable at least partly to the coarser grid resolution of 1°×1° for HadISST1.1 compared with 0.25°×0.25° for OISST. The lower resolution of the HadISST1.1 dataset is not a major issue for many studies of large-scale climate variability.

2) The standard deviations of the SST anomalies are 0.2–0.4°C smaller in the HadISST1.1 dataset than in the OISST dataset. This is likely also attributable at least partly to the coarser grid resolution of the HadISST1.1 dataset. However, the magnitudes of these differences seem larger than could be accounted for solely by the coarser resolution of the HadISST1.1 dataset.

3) The standard deviations of the SST anomalies in the HadISST1.1 dataset are 0.2–0.4°C smaller prior to 1949 than after 1949. This nonstationarity could complicate interpretations of the long HadISST1.1 data record for some studies of climate variability. It is likely attributable mostly to the improved sampling of SST observations in the later time period.

4) There is a large zonal discontinuity of SST in the HadISST1.1 dataset along 179.5°W that results in SST variations that are typically smaller in magnitude by about 0.2°C compared with the adjacent 1° grid cells to the west and east. It appears that this discontinuity becomes noticeable abruptly in 1949.

5) There are additional zonal discontinuities of SST at regular intervals of 4° and 2° of longitude in, respectively, the pre-1949 and post-1949 portions of the HadISST1.1 data record. These discontinuities in zonal first differences of SST are manifest as step-like structures in SST itself, with typical jumps of 0.1°C prior to 1949 and 0.05°C after 1949.

6) There are also meridional discontinuities at intervals of 4° and 2° of latitude in, respectively, the pre-1949 and post-1949 portions of the HadISST1.1 data record. The amplitudes of the meridionally oscillating striations in the standard deviations of meridional first differences are as large or larger than the amplitudes of the zonally oscillating striations in the standard deviations of zonal first differences.

While all of the above issues are significant concerns, we showed in Sec. 2 that the HadISST1.1 dataset is still useful for studies of the large-scale signals associated with short-term climate variability (interannual to decadal time scales). The dataset is inadequate, however, for studies

that require information about spatial derivatives of the SST field. As an example, the analysis in Sec. 5 shows that the HadISST1.1 dataset cannot be used for investigation of mesoscale air-sea interaction (scales of 100–1000 km). Prior to 1949, maps of the standard deviations of the downwind and crosswind SST gradient fields that are the telltale signs of this ocean-atmosphere interaction are corrupted by a checkerboard pattern of artifacts with dimensions of 4° of longitude by 4° of latitude. The problem is more insidious after 1949 if spatial derivatives are estimated by the usual 3-point centered differencing. When the derivatives are estimated with higher resolution from 2-point first differences to compute the SST gradient field on a staggered grid, a checkerboard pattern of artifacts with dimensions of 2° of longitude by 2° of latitude becomes readily apparent. The checkerboard patterns of artifacts in the downwind and crosswind SST gradient fields mask the influence of SST on the overlying wind field that is an important air-sea interaction process on scales of 100–1000 km.

We do not know the reasons for the problems in the HadISST1.1 dataset that have been identified from our analysis. We suspect that they are mostly artifacts of the details of the smoothing and interpolation procedure used to grid the observational SST data. Our hope is that the results presented in this report will motivate a reprocessing of the data to eliminate the artifacts summarized above.

Acknowledgments. The work summarized in this report was supported by the U.S. National Aeronautics and Space Administration.

Contact information: chelton@coas.oregonstate.edu

References

Bond, N. A., M. F. Cronin, H. Freeland and N. Mantua, 2015: Causes and impacts of the 2014 warm anomaly in the NE Pacific. *Geophys. Res. Lett.*, **42**, 3414-3420, doi:10.1002/2015GL063306.

Chelton, D. B., M. G. Schlax, M. H. Freilich and R. F. Milliff, 2004: Satellite measurements reveal persistent small-scale features in ocean winds. *Science*, **303**, 978-983.

Kaiser-Weiss, A., J. Vazquez and M. Chin, 2012: GHRSST User Requirements Document (URD), Version 2.0. National Centre for Earth Observation, Dept. Meteorology, University of Reading, Reference D-06 URD_v02, 42 pp.

O'Neill, L. W., D. B. Chelton, and S. K. Esbensen, 2010: The effects of SST-induced surface wind speed and direction gradients on midlatitude surface vorticity and divergence. *J. Climate*, **23**, 255-281.

Reynolds, R. W., T. M. Smith, C. Liu, D. B. Chelton, K. S. Casey and M. G. Schlax, 2007: Daily high-resolution-blended analyses for sea surface temperature. *J. Clim.*, **20**, 5473-5496.

Small, R. J., S. P. de Szoeke, S.-P. Xie, L. W. O'Neill, H. Seo, Q. Song, P. Cornillon, M. Spall and S. Minobe, 2008: Air-sea interaction over ocean fronts and eddies. *Dyn. Atmos. and Oceans*, **45**, 274-319.

Xie, S.-P., 2004: Satellite observations of cool ocean-atmosphere interaction. *Bull. Amer. Meteor. Soc.*, **85**, 195-208.